Journal of Energy Storage 61 (2023) 106808

Contents lists available at ScienceDirect

Journal of Energy Storage

journal homepage: www.elsevier.com/locate/est

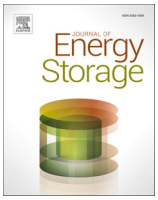

Research papers

Numerical analysis of a flywheel energy storage system for low carbon powertrain applications

Shahed Motaman [a,b], Mahmoud Eltaweel [a], Mohammad Reza Herfatmanesh [a,*], Tobias Knichel [c], Andrew Deakin [c]

[a] School of Physics, Engineering and Computer Science, University of Hertfordshire, United Kingdom
[b] School of Computing and Engineering, University of Derby, United Kingdom
[c] PUNCH Flybrid, United Kingdom

ARTICLE INFO

Keywords:
Computational fluid dynamics
Model validation
Rotor skin friction coefficient
Taylor-Couette flow
Windage loss
Flywheel energy storage

ABSTRACT

Flywheel energy storage has emerged as a viable energy storage technology in recent years due to its large instantaneous power and high energy density. Flywheel offers an onboard energy recovery and storage system which is durable, efficient, and environmentally friendly. The flywheel and the housing surface temperatures can be considerably influenced by the friction induced windage losses associated with non-vented airflows in the air-gap of a high-speed rotating flywheel. Many engineering applications have been interested in the features of radial and axial air-gap flows. The flow within the annulus of a flywheel is extremely complicated. This study has developed a numerical technique using ANSYS Fluent solver to model turbulent Taylor vortices formation and oscillation for thermal performance evaluation, and windage loss prediction of high-speed flywheel storage systems, operating under atmospheric and partial vacuum conditions. The numerical model has been experimentally validated with good accuracy. Several rotational speeds and pressures were investigated experimentally and numerically. The results demonstrated that a 40 % reduction in the operating pressure can reduce the flywheel surface temperature and windage loss by 20 % and 30 %, respectively. Consequently, a partial vacuum environment can achieve better energy conversion efficiencies provided an appropriate bearing seal is achieved to maintain the pressure inside the housing. The investigated flywheel energy storage system can reduce the fuel consumption of an average light-duty vehicle in the UK by 22 % and decrease CO_2 emission by 390 kg annually.

1. Introduction

The push for decarbonisation and sustainability has sparked interest in developing energy storage technologies to avert irreversible climate change [1]. Climate change is a major worldwide issue that must be addressed immediately. Global greenhouse gas emissions need to be reduced by 41–72 % by the year 2050 compared to 2010 levels to keep the temperature change below 2 °C [2]. According to the World Health Organisation (WHO), urban air pollution has been identified as the primary cause of premature deaths for 7 million people annually worldwide [3]. Consequently, automakers are facing a technological challenge to simultaneously increase engine efficiency and reduce exhaust emissions.

A significant portion of the engine's power output is lost due to frequent braking in the form of excess heat in brake discs. To harvest this excess mechanical energy from the engine, a regenerative braking system was introduced in 1967. American Motors introduced and tested this technology on their concept electric car "Amitron" [4]. This concept car was equipped with regenerative braking technology to harness excess mechanical energy during braking to charge an onboard battery storage system. This technology has been further developed and implemented in modern hybrid vehicles by various automakers in the last two decades to meet ever stringent emissions legislation. The hybrid vehicles with the Flywheel Energy Storage System (FESS) are far superior to their battery-powered counterparts in terms of cost, volume, efficiency and weight [5].

FESS is gaining popularity lately due to its distinctive benefits, which include a long life cycle, high power density, minimal environmental impact and instantaneous high power density [6]. Flywheel Kinetic Energy Recovery System (KERS) is a form of a mechanical hybrid system in which kinetic energy is stored in a spinning flywheel, this technology is being trialled by selected bus, truck and mainstream automotive

* Corresponding author.
E-mail address: m.r.herfatmanesh@herts.ac.uk (M.R. Herfatmanesh).

https://doi.org/10.1016/j.est.2023.106808
Received 5 December 2022; Received in revised form 26 January 2023; Accepted 30 January 2023
Available online 11 February 2023

companies [7]. Flywheel storage systems can supply instantaneous high power for short periods of time [8]. During braking, the excess energy is transmitted to the flywheel via a Continuously Variable Transmission (CVT) gearbox and is stored as kinetic energy in the flywheel. A motor/generator is directly connected to the flywheel rotor to charge and discharge energy in hybrid and electric vehicles [9]. The storage capacity depends on the size and rotational speed of the flywheel, the latter is more significant since the storage capacity is proportional to the square of the flywheel speed. The use of composite materials allows for faster rotational speeds and higher power densities than equivalent battery energy storage systems. High power density is desirable in vehicles that require a large peak power when accelerating and a large power becomes available for storage in a short period of time when decelerating or braking [10].

Consequently, flywheels are often composed of an external carbon fibre composite rim press fit onto a high-strength steel hub to withstand the stresses induced due to high rotational speeds. Generally, flywheel systems are designed to deliver up to 130 kWh of energy [11]. Although higher rotational speeds allow for more energy to be recovered, more heat is generated within the flywheel annulus due to windage losses (i.e. frictional losses). Under a steady-state operation, the excess heat may soften the epoxy within the carbon fibre composite rim, thus compromising its mechanical properties in particular its tensile strength [12,13]. In addition, the excess heat can also alter the mechanical properties of the steel hub through localised thermal stress and deformation, leading to crack formation and propagation thus premature burst failure [12]. Therefore, in such closed and non-vented systems, the FESS must be operated under partial or high vacuum to reduce the frictional losses thus heat generation and dissipation.

The intensity of the windage loss is a function of the flywheel rotational speed, air-gap (annulus) dimension and operating pressure [13,14]. The size of the air-gap is an important factor when designing a flywheel energy storage system [14,15] which is dependent on various parameters including flywheel speed and expansion rate at high speeds [15,16]. The rotation of an enclosed flywheel creates a complex air flow within the air-gap, resulting in heat generation due to frictional losses. The flow characteristics are dependent on the flywheel speed, outer rim surface roughness, air-gap size and properties of the working fluid [16]. Couette and Taylor determined flow viscosity and flow stability in the annulus of two concentric cylinders, consequently, this type of flow is commonly referred to as Taylor-Couette flow [16,17]. Furthermore, Taylor-Couette flow is also present in high-speed electrical machines in particular electric motors, thus windage loss and heat transfer study in such machines has been the subject of several numerical and experimental investigations [18,19].

Flow characteristics within the annulus of two concentric cylinders can be determined by Taylor number. Taylor identified a critical number ($Ta_c = 41.3$) below which flow is considered as laminar Couette and as the rotational speed increases, the flow regime changes from laminar or azimuthal Taylor vortices to unstable and turbulent flow [20]. Gollub and Swinney; and Fenstermacher et al. reported that this type of flow initially develops as a periodic flow regime with a specific axial wavelength followed by a sharp reversible transition to aperiodic flow [21,22].

Another parameter that defines the air flow regime within the flywheel air-gap is the Knudsen number (Kn) which is related to the molecular mean free path (λ) and physical length scale (L) of the flow domain. This dimensionless parameter is defined by the following expression:

$$Kn = \frac{\lambda}{L} \tag{1}$$

where the molecular mean free path (λ) is defined by the following expression:

$$\lambda = \frac{\nu\sqrt{\pi}}{\rho\sqrt{2RT}} \tag{2}$$

where ν is the fluid kinematic viscosity (m^2/s), ρ is the fluid density (kg/m^3), T is the absolute temperature (K) and R is the gas constant. The molecular mean free path is defined as the average distance travelled by the gas molecules between collisions. Flow can be categorised into continuum ($Kn < 0.01$), slip ($0.01 < Kn < 3$) and free molecule ($Kn > 3$) flows [13]. The continuum fluid is considered a Newtonian viscous fluid in which Navier-Stokes momentum equations can be applied. Knudsen number is particularly important for flow analysis under medium or hard vacuum to ensure flow remains continuum.

The heat transfer within the annulus of concentric cylinders and systems of such like is considerably affected by Taylor-Couette flow [19]. Gazley was among the early researchers who examined the heat transfer in the annulus of concentric cylinders [23]. Numerous theoretical and experimental investigations of heat transfer in the annulus of concentric cylinders have been conducted by many researchers. Becker and Kaye; and Aoki et al. [24,25] preformed a series of experimental studies on heat transfer in the annulus of concentric cylinders in the absence of axial cross flow. Tachibana et al. [26] investigated the effect of air-gap size on heat generation and dissipation within the air-gap of an electric motor. Howey et al. [27] also investigated the effect of air-gap size on the convective heat transfer rate of laminar and turbulent swirling air flows in the annulus of high-speed electric motors. They used non-dimensional heat transfer parameters to calculate surface convective heat transfer coefficients for thermal modelling of both radial-flux and axial-flux electrical machines.

Due to the complex structure of flywheel housing as well as safety concerns, it is rather difficult to measure the flywheel rim and hub surface temperatures and thus the convective heat transfer within the air-gap. Temperature measurements are often performed by infrared thermocouples which are generally capable of single point measurement either on the flywheel surface or within the air-gap [14]. However, such devices are not capable of measuring spatial and temporal temperature distribution within the system. Therefore, Computational Fluid Dynamics (CFD) can be used to analyse such complex systems.

There are very few CFD investigations reported in the literature on the thermal analysis of flywheels under atmospheric and partial vacuum operating conditions. The majority of the CFD investigations are focused on the thermal analysis of high-speed electric motors [28,29].

Anderson et al. [28] performed a CFD investigation on the heat transfer of a high-speed electric motor. They proposed a novel heat transfer correlation suitable for large axial Reynolds numbers, large Taylor numbers and small annular gap flows. Viazzo and Poncet [30] investigated numerically and experimentally the gas flow stability and heat transfer in an annular channel of a high-speed electric motor. In addition, Hosain et al. [19] examined numerically the Taylor-Couette flow inside the annulus of rotating electrical machines. They validated their CFD results with the correlations available in the literature and reported periodic thermal distribution alongside the stator surface.

As mentioned earlier, the majority of previous CFD investigations were focused on thermal management and heat transfers of high-speed electrical machines under atmospheric conditions. Therefore, there exists a lack of CFD investigation on flow analysis of flywheel energy storage systems to better understand the heat transfer and thermal management of such complex systems.

In this work, three-dimensional computational fluid dynamics modelling was carried out to investigate the effect of partial vacuum on the aerodynamic performance of an enclosed flywheel energy storage system designed and manufactured by PUNCH Flybrid, with a high operating speed of over 14,000 rpm. Thermal analysis of the flow within the air-gap was performed to investigate the spatial temperature distribution within the flywheel assembly. The temperature of the carbon fibre ring is an important factor since excessive temperatures may cause

the resin between the fibres to evaporate, leading to premature mechanical failure. To the best of the authors' knowledge, this is one of the first experimental and numerical attempts to investigate the flow and thermal analysis of a flywheel storage system. The effect of using a flywheel in light-duty vehicles to reduce carbon emissions was also studied with the view to highlight the effectiveness of this technology for transport decarbonisation.

2. Experimental validation

2.1. Flywheel test

The experimental setup used to test the flywheel system is shown in Fig. 1. The flywheel assembly is placed inside a stainless-steel containment as part of the lab safety code. The flywheel is connected, via a fixed ratio transmission, to an ABB induction motor, M3EH 160D 4, with the nominal power of 136.5 kW and maximum rotational speed of 6500 rpm, capable of rotating the flywheel up to 40,000 rpm. The flywheel used in this study is made from two parts: an inner steel hub and an outer reinforced carbon-fibre ring. PUNCH Flybrid has designed and manufactured the flywheel to be used for automotive applications. Tables 1 and 2 show the flywheel dimensions and the experimental and numerical test plan, respectively. The flywheel's maximum rotational speed was set at 14,000 rpm in this investigation.

An electric vacuum pump was used to create a partial vacuum inside the flywheel cavity while a closed oil circuit cooling system was used to maintain a safe working temperature for the shaft and bearings. Five thermocouples were used to measure surface temperature at various locations. The Infrared (IR) temperature sensor was used to measure the surface temperature of the flywheel carbon fibre rim while the other four temperature sensors were used to monitor the temperature of the flywheel housing, oil inlet and outlet temperatures and the ambient temperature. The ambient temperature was kept at a constant temperature of 24 °C during testing. The flywheel speed increased with increments of 1000 rpm during testing to allow the system temperature to stabilise at each set point. Temperature stability was defined as when IR temperature data changed <5 % in 60 s. All temperature readings were collected at each set point once the stabilisation criterion was met, this data was used to validate the CFD model.

Table 1
Flywheel dimensions.

Component	Dimensions (mm)
Housing diameter	320
Flywheel diameter	260
Flywheel width	130
Air-gap size	1.33

Table 2
Experimental and numerical test plan.

Studied cases	Test 1	Test 2	Test 3	Test 4	Test 5
Flywheel speed (rpm)	5000	7000	9000	12,000	14,000
	1000	1000	1000	1000	1000
Air pressure (mbar)	800	800	800	800	800
	600	600	600	600	600

3. Flywheel frequency analysis

Frequency analysis for mechanical resonance is an important consideration in the design of a FESS. Resonance occurs when the natural frequency of a system matches the frequency of an external force applied to it [31]. Resonance can occur in a FESS if the rotational frequency of the flywheel coincides with the frequency of an external vibration or shock. This can result in structural failure or decreased system efficiency [32]. To prevent or mitigate resonance in the tested FESS, frequency analysis was conducted using SolidWorks to determine the natural frequencies of the system. High density steel alloy was used for the flywheel hub and shaft, while carbon fibre was used for the flywheel rim. The frequency analysis determined that the flywheel's first natural frequency is approximately 235 Hz, while the third and fifth natural frequencies were found to be 310 Hz and 965 Hz, respectively. Since the mechanical frequency of the motor used is 101.1 Hz, it can be inferred that the system's operating frequency is lower than the flywheel's natural frequencies, thus, the system is unlikely to experience any mechanical resonance.

4. Thermal conductivity measurement

To identify the thermal conductivity and specific heat capacity of the

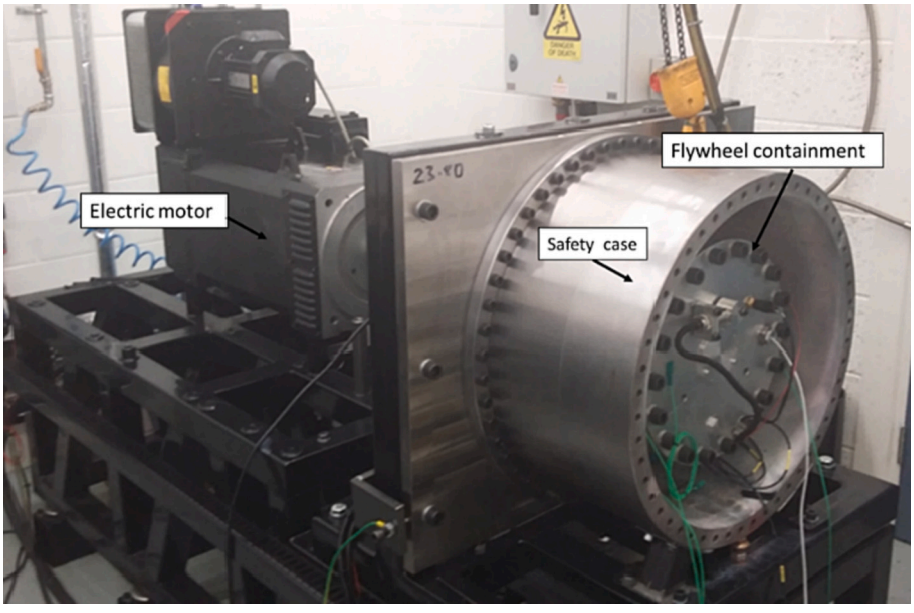

Fig. 1. Flywheel experimental setup.

carbon fibre material, which is required as an input for the CFD simulations, a Hot Disk (TPS 2500 S) thermal conductivity analyser was used as shown in Fig. 2. Since the carbon fibre rim has an anisotropic structure, its thermal properties are dependent on the carbon fibre arrangement in the composite matrix. In this setup, the Hot Disk sensor is sandwiched between two sheets of material. The temperature of the sensor increases by running a current through it (between a fraction of a degree up to several degrees) thus generating heat. Subsequently, the amount of heat per unit time and unit area of the sample is recorded [33]. The sensors used in this study were a Kapton 5465 (0.0032 m radius) and a gold cell sample holder (0.0095 m radius and 0.005 m thickness) for thermal conductivity and specific heat capacity measurements, respectively. The carbon fibre composite was cut into circular samples of 0.064 m diameter and 0.0032 m thickness to fit the dimensions of the sensors for the thermal conductivity and specific heat capacity measurements. The top and side views of the Hot Disk sample and sensor holder are shown in Fig. 3. The thermal conductivity measurements were carried out at room temperature, 24 °C.

To ensure that the assumption of an infinite sample domain was satisfied, and the heat was not penetrating through the sample in the axial direction, two carbon fibre samples were stacked on top of each other on either side of the sensor. The measurements were repeated ten times to ensure the accuracy and repeatability of the results.

5. Numerical modelling methodology

Fig. 4 shows the three-dimensional computational domain used for the flywheel geometry under investigation. The computational analysis uses the same flywheel geometry and size as the flywheel tested by PUNCH Flybrid. Due to the symmetrical nature of the flywheel geometry and to reduce the computational time and cost, only half of the computational domain is considered. Furthermore, since the flow within the air-gap is repeated periodically, the geometry was further simplified by slicing a 72-degree section and applying periodic boundary conditions at each end of the geometry as shown in Fig. 5.

In total, twenty different simulations were performed to simulate the performance of the flywheel under different operating conditions and rotational speeds as previously mentioned in Table 2. The air-gap was modelled as a moving fluid with different rotational speeds applied to the fluid domain. To monitor and record flow properties within the air-gap, an axial probe line was created at the centre of the flywheel air-gaps as shown in Fig. 6. The probe was used to monitor velocity fluctuations inside the flywheel air-gap. ANSYS Fluent flow solver was used to solve Reynolds-Averaged Navier–Stokes (RANS) equations (i.e. partial differential equations governing fluid flow) for compressible and Newtonian fluids.

Due to the complex nature of the flywheel geometry, a mixture of hexahedral and tetrahedral cells were applied on different parts of the flywheel assembly as shown in Fig. 7. The flywheel annulus was divided into two parts: air-gap top which covers the area on top of the flywheel carbon fibre rim and air-bottom which covers the sides of the flywheel and the inside of the steel hub. In total, 7.5 million elements were used for the base mesh. To improve the accuracy of the numerical results, mesh independence test was performed. Table 3 illustrates the mesh size applied on different flywheel zones.

The k-ω SST turbulence model with viscous heating was selected to solve Reynolds stress tensors for a highly turbulent air flow within the flywheel air-gap. This turbulence model is recommended for swirling and recirculating flows with high Reynolds numbers. Moreover, the SST model is a hybrid two-equation model that combines the advantages of both k-ε and k-ω models. According to the review of turbulence models given by Versteeg and Malalasekera [34], the k-ω SST turbulence model is particularly well suited for narrow gap annuli with high swirl flow and in particular where viscous sublayers need to be resolved. To fully resolve the viscous sublayers, required to study heat transfer between the air and the flywheel, automatic wall treatment was used to satisfy the non-dimensional wall distance, y^+ [35]. In this configuration, the near-wall treatment is handled automatically, therefore, the air-gap was meshed to achieve a y^+ value of around 30.

Aerodynamic flow types are typically divided into three categories: continuum flow, slip flow and free molecular flow. In each case, the transition between each state is identified by the Knudsen number. The Knudson number at 14,000 rpm and under atmospheric and partial vacuum pressures of 800 and 600 mbar is 4511×10^{-8}, $11{,}127 \times 10^{-8}$ and $10{,}526 \times 10^{-8}$, respectively. Thus, the flow can be considered a continuum fluid regime, allowing the use of RANS equations. The following assumptions were made for the CFD model employed in this study:

- The computation is performed using double precision.
- The solver employed is pressure-based.
- The k-ω SST turbulence model with viscous heating is selected to solve RANS equations.
- The energy equation is included in the solution process.
- The coupled solution method is utilised.
- The pressure discretisation scheme is of second-order accuracy.

Fig. 2. Hot Disk thermal conductivity analyser.

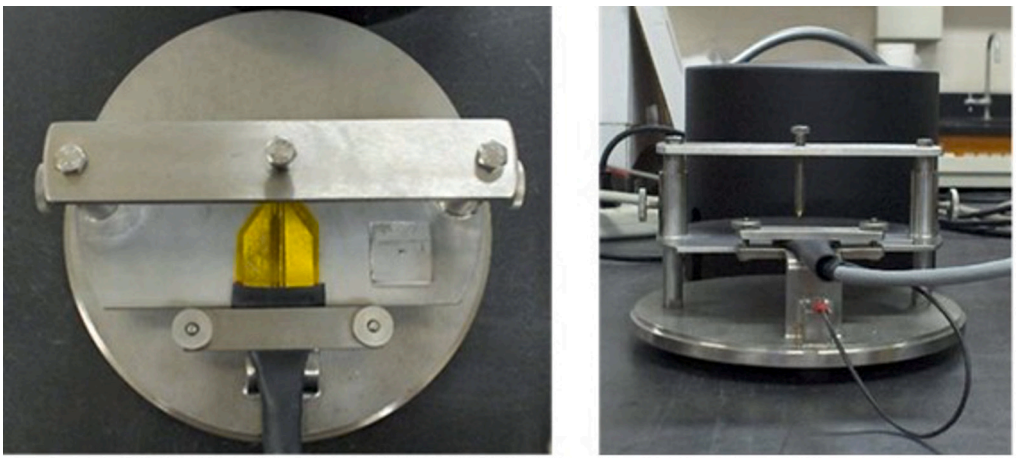

Fig. 3. Hot Disk sample and sensor holder.

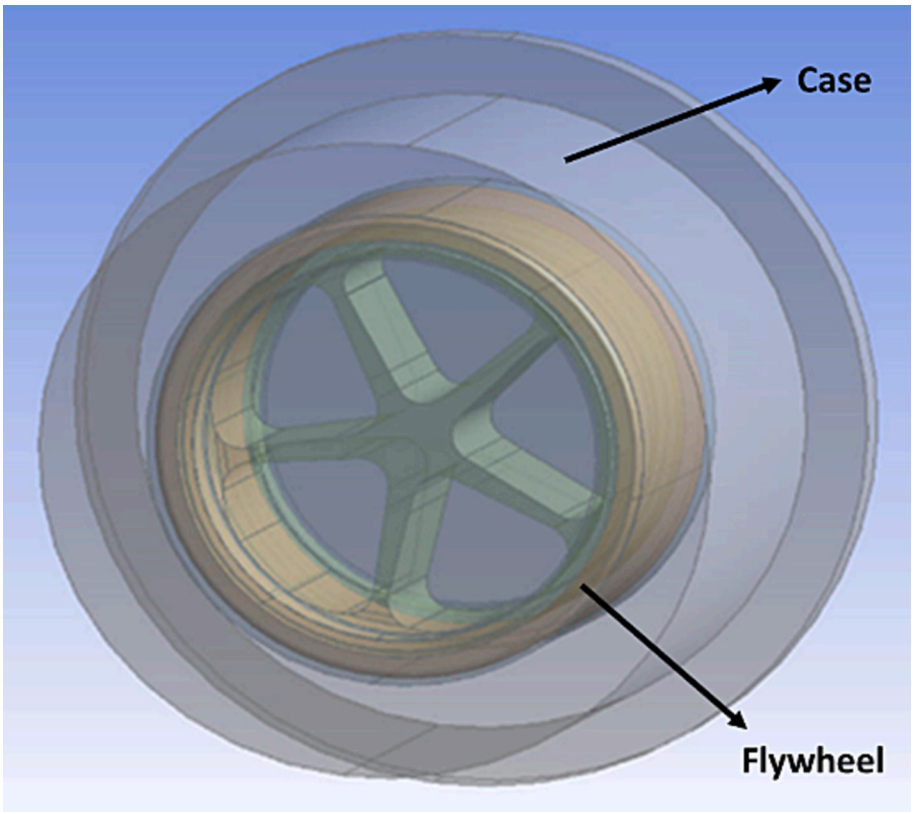

Fig. 4. Original flywheel geometry.

- The QUICK scheme is employed for the discretisation of density, momentum, turbulent kinetic energy, specific dissipation rate and energy.

Air was modelled as a compressible ideal gas with variable viscosity based on Sutherland's law since Sutherland's law is well suited for high-speed compressible flows [36]. Compressibility becomes important for high-speed flows where significant changes in velocity, pressure and temperature cause variations in density. To model the heat transfer between the solid and fluid domains, non-conformal coupled mapped wall condition was applied at the zone interfaces to allow mass and heat transfer across the boundaries.

The thermal boundary condition for the flywheel case was set to convection with the free stream temperature of 24 °C and heat transfer coefficient of 30 $W/m^2.K$, replicating the overall thermal boundary condition of the flywheel case during the experiments. The thermal properties of different flywheel components are listed in Table 4. The initial temperature of the flywheel assembly was set to 24°C and the solution convergence criteria for velocity, continuity and turbulence k-ω residuals were set to be 10^{-6} and for energy to be 10^{-8}. The boundary conditions for each CFD zone are listed in Table 5.

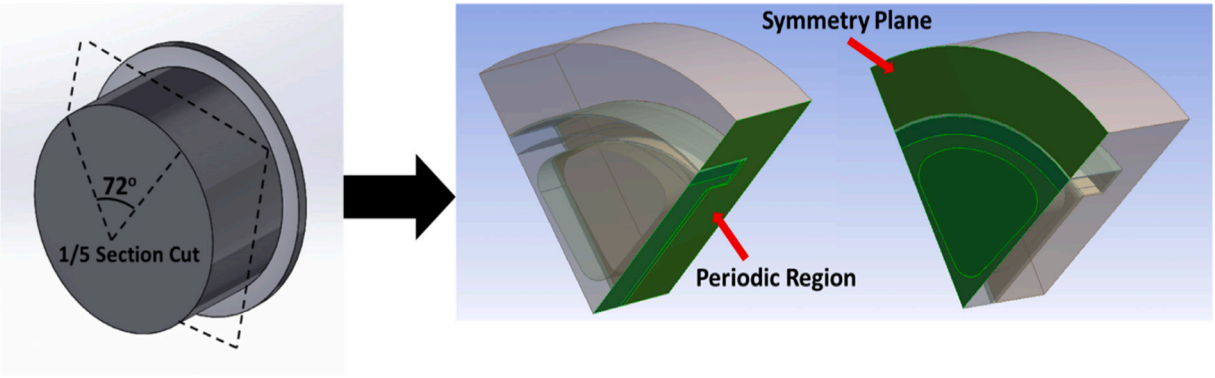

Fig. 5. Simplified flywheel geometry with symmetry plane and periodic regions.

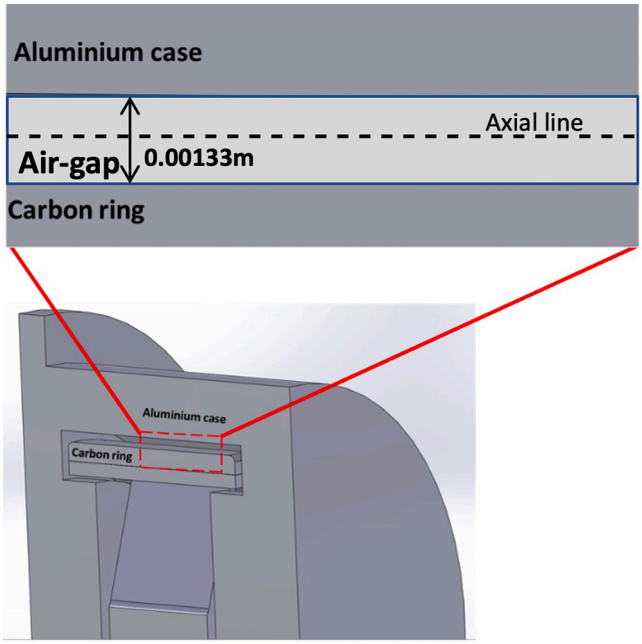

Fig. 6. Axial probe line within the flywheel air-gap.

6. Mesh sensitivity analysis

The average temperature of flywheel components as a function of mesh element size at the rotational speed of 14,000 rpm and under atmospheric conditions has been identified. As shown in Fig. 8, the average temperature of flywheel components remained almost constant for mesh 2, 4 and 5. The mesh independence study demonstrated that further refinement beyond mesh 2 only increases the computational time and cost with negligible improvements in prediction accuracy of the CFD model, thus, mesh 2 with 9.3 million cells was selected as the optimum mesh for this investigation.

Table 3
Mesh sensitivity analysis.

Mesh zone	Mesh 1 (Baseline)	Mesh 2	Mesh 3	Mesh 4	Mesh 5
	Element size (mm)				
Case	3	2	2	2	2
Air-gap-top	0.33	0.19	0.14	0.19	0.19
Air-bottom	2	1	1	0.8	0.5
Carbon-fibre-rim	3	2	2	2	2
Steel-hub	3	2	2	2	2
Total cell number	7.5 million	9.3 million	11.5 million	12.4 million	14.2 million

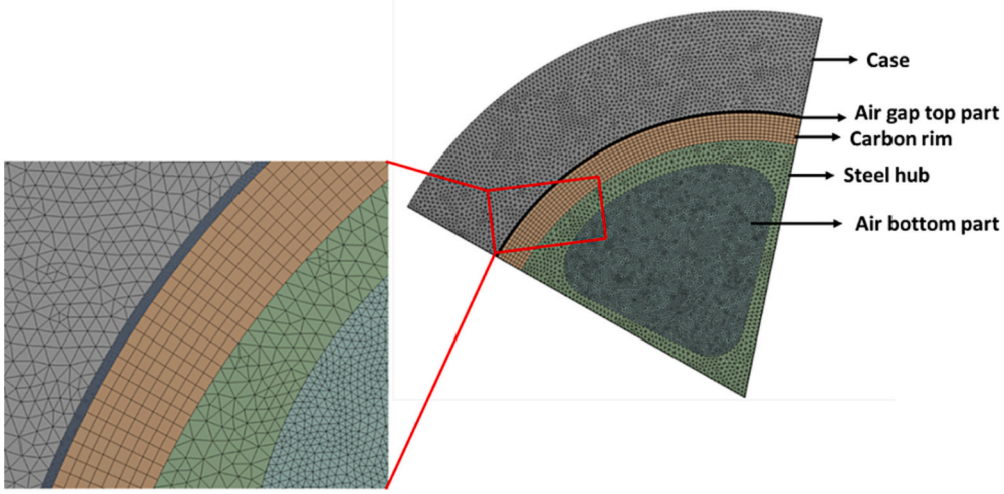

Fig. 7. Tetrahedral and hexahedral mesh used for the baseline.

Table 4
Thermal properties of flywheel components.

CFD zone	Material	Density (kg/m^3)	Specific heat (J/kg.K)	Thermal conductivity (W/m.K)
Air-gap	Air	Ideal gas	1006.43	0.0242
Flywheel-rim	Carbon fibre	1473	645	1.40
Flywheel-hub	Steel	8030	502.48	16.27
Case	Aluminium	2719	871	202.40

Table 5
CFD boundary conditions.

CFD zone	Boundary conditions
Flywheel	Wall motion: Moving Reference Frame (MRF) Shear condition: No-slip Thermal: Initial temperature 24°C
Air	No inlet or outlet Viscosity calculated using Sutherland's three-equation model Thermal: Initial temperature 24°C
Case	Wall motion: stationary Shear condition: No-slip Thermal: Initial temperature 24°C, free stream temperature 24°C and convective heat transfer coefficient 30 W/m^2 K

7. Results and discussion

The average carbon fibre surface temperatures at different rotational speeds and operating pressures are shown in Fig. 9. The experimental and numerical results show a good level of agreement, with both methods displaying similar trends. However, it should be noted that the numerical results tend to underpredict the carbon fibre surface temperature at low rotational speeds under atmospheric conditions, and overpredict at high rotational speeds under partial vacuum conditions. These deviations can be attributed to the simplified geometry used in the numerical model, which does not consider the flywheel shaft, bearing cooling and the thermal mass of the additional safety containment, mounting brackets and frame as shown in Fig. 1. Despite these limitations, the differences between the experimental and numerical results fall within the predefined 15 % uncertainty range.

Figs. 10 and 11 present the linear velocity and total temperature distributions across the air-gap and flywheel carbon fibre rim at a rotational speed of 5000 rpm and pressure of 1000 mbar, respectively. These figures reveal the presence of periodic spiral Taylor vortices within the air-gap and axisymmetric toroidal rolls on the carbon fibre top surface. These results provide insight into the flow dynamics and thermal characteristics of the system under investigation.

The flow pattern within the air-gap of the FESS is characterised by the Taylor and Reynolds numbers, which are functions of the air-gap size, kinematic viscosity and angular velocity [19]. These parameters determine the flow regime within the air-gap, which can be classified into three regimes based on the critical Taylor number [20]:

$T_a < 41.3$ Laminar Couette flow

$41.3 < T_a < 400$ Flow with wavy Taylor vortices (WTV)

$T_a > 400$ Turbulent Taylor vortex flow (TTVF).

The Taylor number is defined as the ratio of inertial forces to viscous forces within the flow, and can be calculated through the following expression [20]:

$$T_a = \frac{U_i \times d}{\upsilon} \times \left(\frac{d}{r_i}\right)^{0.5} \quad (3)$$

where U_i is the flywheel peripheral velocity, d is the flywheel air-gap size (m), r_i is the flywheel outer radius (m) and υ is the kinematic viscosity of the working fluid (m^2/s).

The rotational Reynolds number is defined by the following expression:

$$R_e = \frac{r_i \times \omega \times d}{\upsilon} \quad (4)$$

where ω is the flywheel angular velocity.

The flow pattern inside the flywheel air-gap changes as the Reynolds

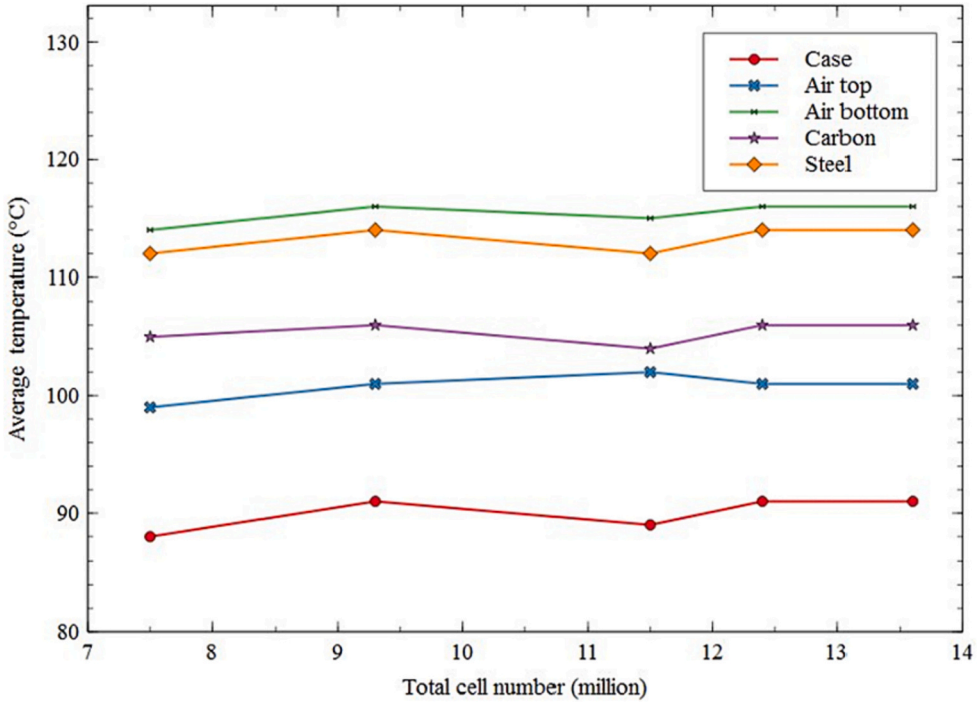

Fig. 8. Average temperature vs total number of cells at the rotational speed and pressure of 14,000 rpm and 1000 mbar, respectively.

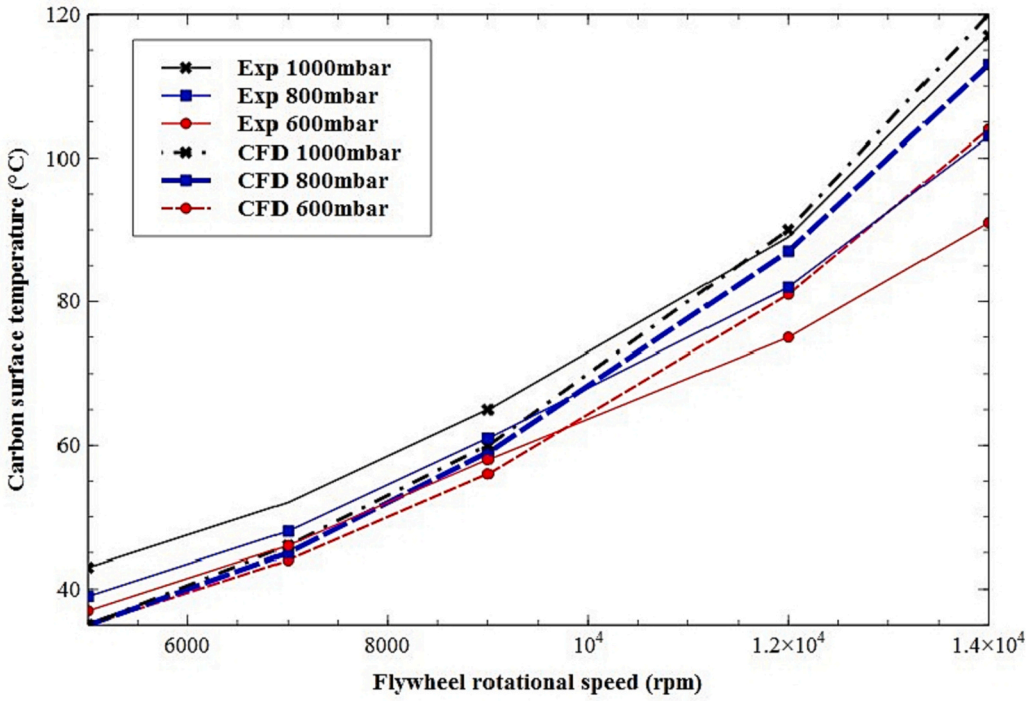

Fig. 9. Experimental and numerical average carbon fibre surface temperature at different rotational speeds and pressures.

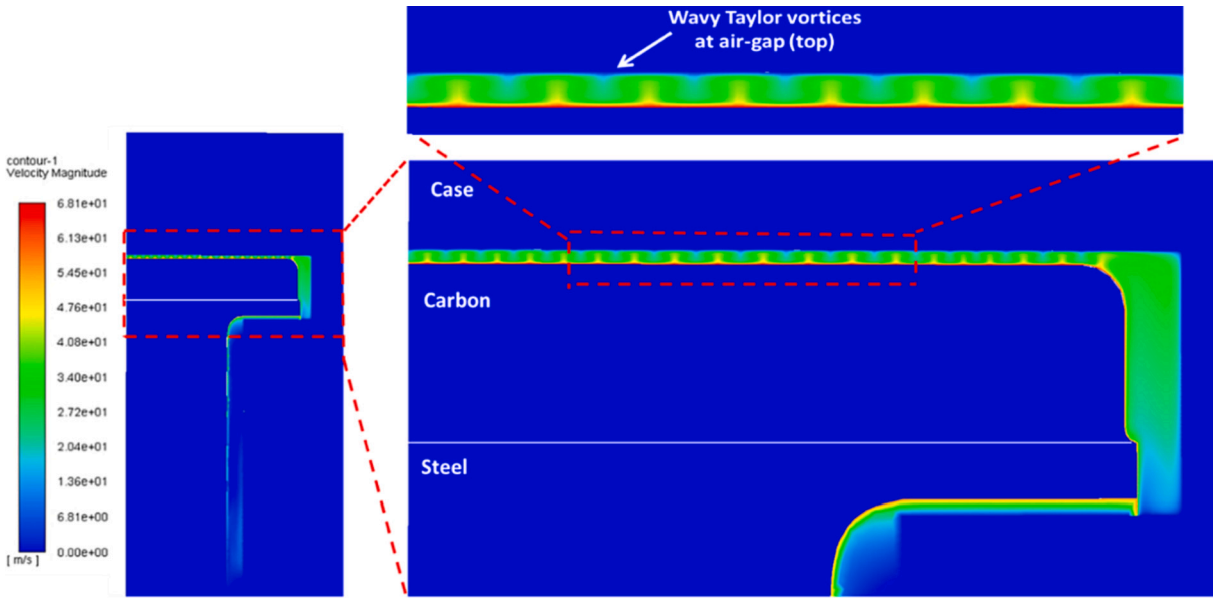

Fig. 10. Linear velocity contour plot with the air-gap size of 0.00133 m at the rotational speed and pressure of 5000 rpm and 1000 mbar, respectively.

number increases above the critical Reynolds number, R_{ec}. The critical Reynolds number associated with the onset of Taylor vortices is a function of the radius ratio of concentric cylinders $\eta = \frac{r_i}{r_o}$ in which r_o is the inner radius of the case (m) [37]. When the Reynolds number is below R_{ec}, the flow is considered laminar with pure azimuthal Couette flow. However, when the Reynolds number is slightly below or equal to R_{ec}, the flow pattern changes to time-independent toroidal vortices, known as Taylor Vortex Flow (TVF). As the Reynolds number increases further, the flow becomes unstable and time-dependent, resulting in the formation of periodic spiral and azimuthal Wavy Taylor Vortices (WTV). Further increases in Reynolds and Taylor numbers lead to the formation of high-frequency Modulated Wavy Taylor Vortices (MWTV) and eventually fully Turbulent Taylor Vortex Flow (TTVF) [37]. The structure of fully turbulent Taylor vortices becomes increasingly complex as the Reynolds number increases, eventually disappearing and becoming undetectable.

The critical Reynolds number, which is associated with the onset of Taylor vortices, has been determined experimentally by other researchers for different radius ratios, as shown in Table 6. In this study, with a radius ratio of 0.98, the critical Reynolds number is estimated to be approximately 200. The Taylor and Reynolds numbers at different rotational speeds and operating pressures are depicted in Figs. 12 and 13, respectively. The results indicate that, apart from the test case at 5000 rpm and 600 mbar, the flow pattern inside the air-gap is turbulent

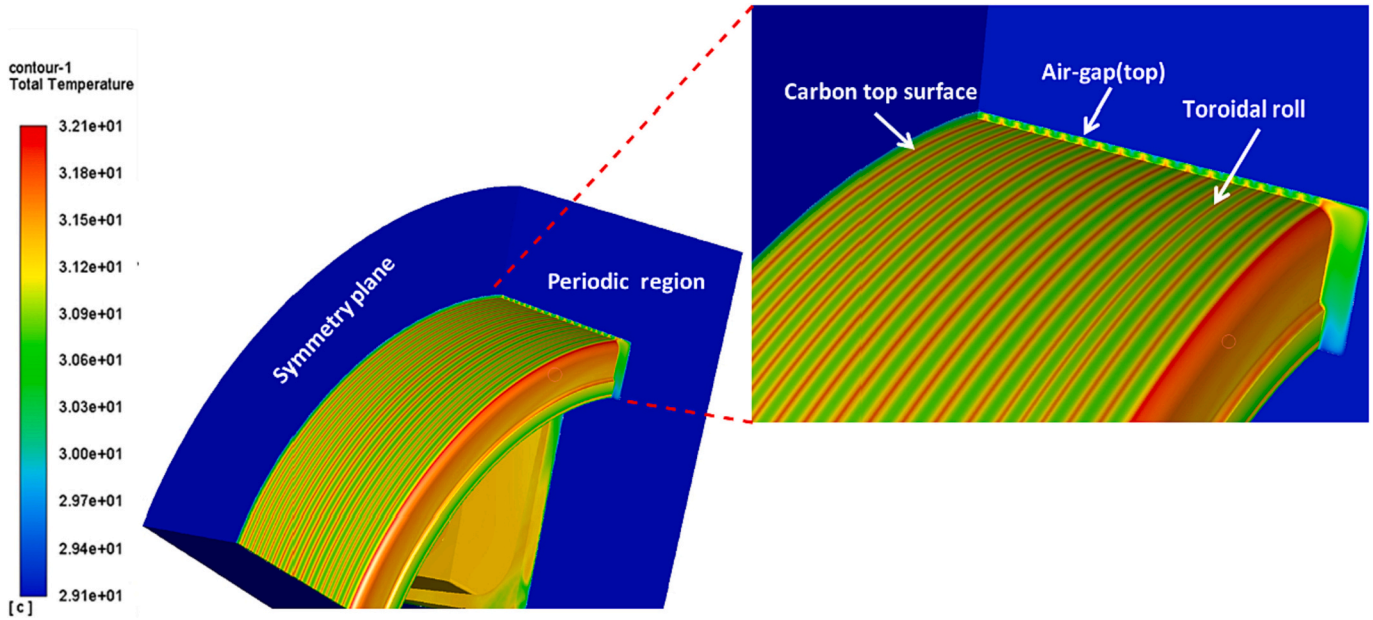

Fig. 11. Temperature distribution with axisymmetric toroidal rolls formed on carbon fibre top surface at the rotational speed and pressure of 5000 rpm and 1000 mbar, respectively.

Table 6
Critical Reynolds number for different radius ratios [37].

Flywheel radius ratio (η)	Critical Reynolds number
0.68	79
0.85	125
0.98	200

with Taylor vortices for all the tested rotational speeds and pressures. Additionally, all Reynolds numbers in Fig. 13 are above the critical Reynolds number, indicating that the flow regime within the air-gap is time-dependent and characterised by the presence of periodic spiral WTV.

The velocity vector plots of turbulent Taylor vortices at rotational speeds of 5000, 9000 and 14,000 rpm and operating pressures of 600 and 1000 mbar are presented in Fig. 14. The spiral, wavy Taylor vortices are observed to be symmetrical in the axial direction within the air-gap, where increase in the rotational speed and inertial forces overcome the viscous forces. The figure illustrates that the Taylor vortices are more stretched at lower speeds and pressures (5000 rpm and 600 mbar) compared to higher speeds and pressures (9000 and 14,000 rpm).

Fig. 15 illustrates the wavelength of the periodic wavy Taylor vortices at different rotational speeds and pressures. The wavelength at 5000 rpm and 600 mbar is measured to be 0.007 m which is higher than the wavelength of 0.004 m at 14,000 rpm and 1000 mbar. This is mainly attributed to the fact that at higher rotational speeds flow becomes fully turbulent with more compact Taylor vortex cells, thus a shorter distance is travelled by the vortices.

The transient time-dependent WTV formation within the flywheel annulus is shown in Fig. 16. The temperature contour plots from the

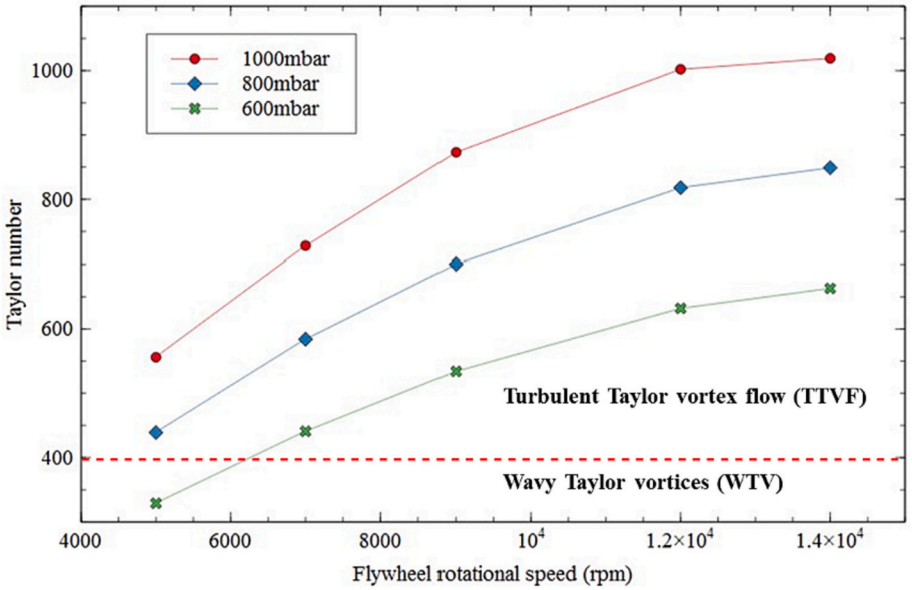

Fig. 12. Air-gap Taylor number at different flywheel rotational speeds and pressures.

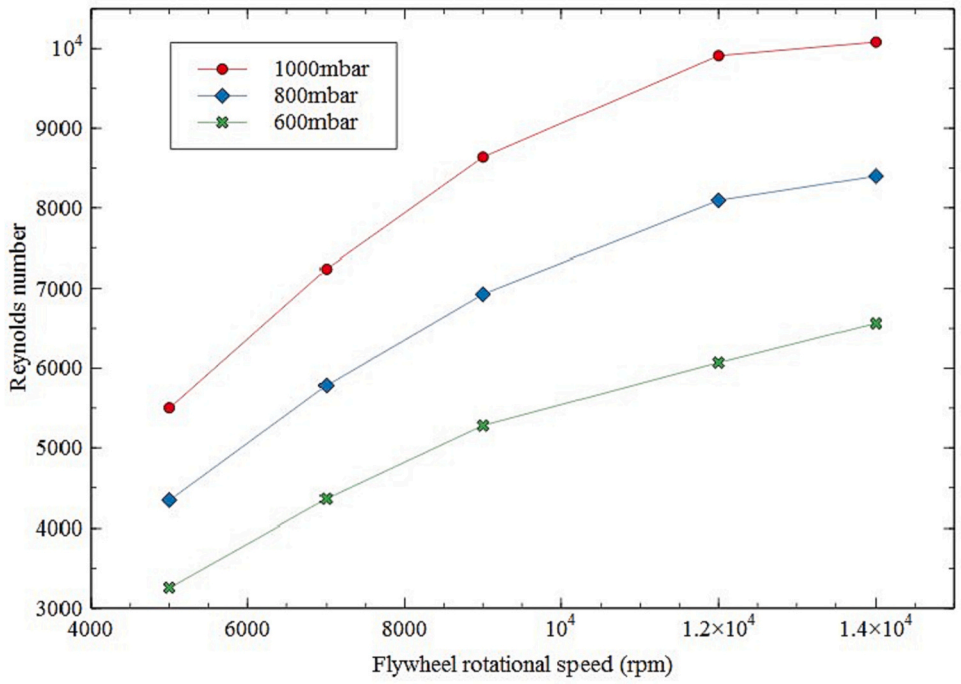

Fig. 13. Air-gap Reynolds number at different flywheel rotational speeds and pressures.

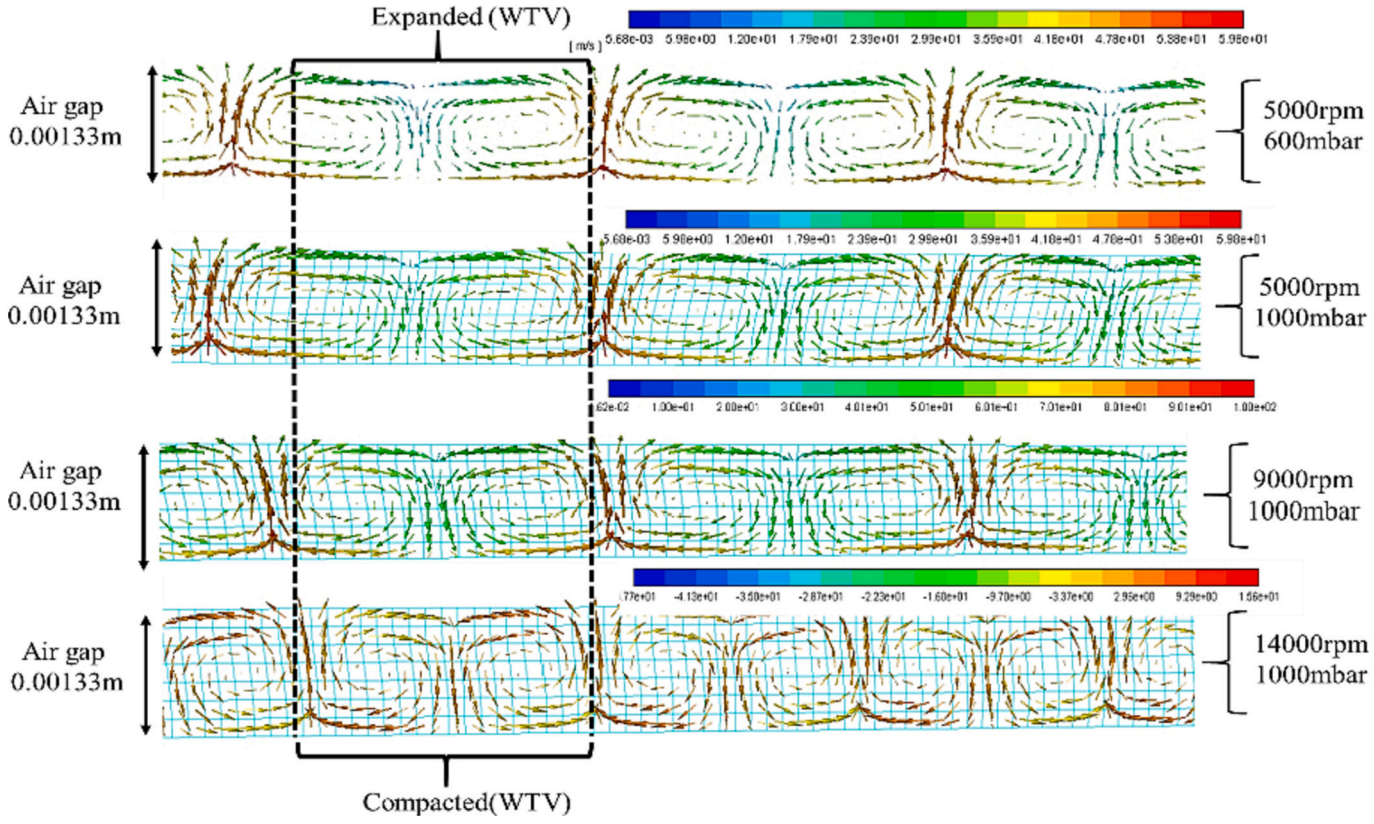

Fig. 14. Velocity vector plots of the periodic spiral WTV in the flywheel air-gap at different rotational speeds and pressures.

onset of the simulation up to 0.06 s are presented at the rotational speed of 5000 rpm and operating pressure of 1000 mbar. The formation of the first toroidal rolls in the axial direction and on the edge of the carbon fibre surface is depicted in the image sequence at $t = 0.0066$ seconds. As the simulation progresses, more axisymmetric toroidal rolls are observed to form, as seen in the image sequences up to $t = 0.026$ seconds. By $t = 0.033$ seconds, fully developed periodic Taylor vortices are observed to move in the axial direction within the flywheel annulus, as depicted in the image sequences at $t = 0.046$ seconds and $t = 0.053$ seconds.

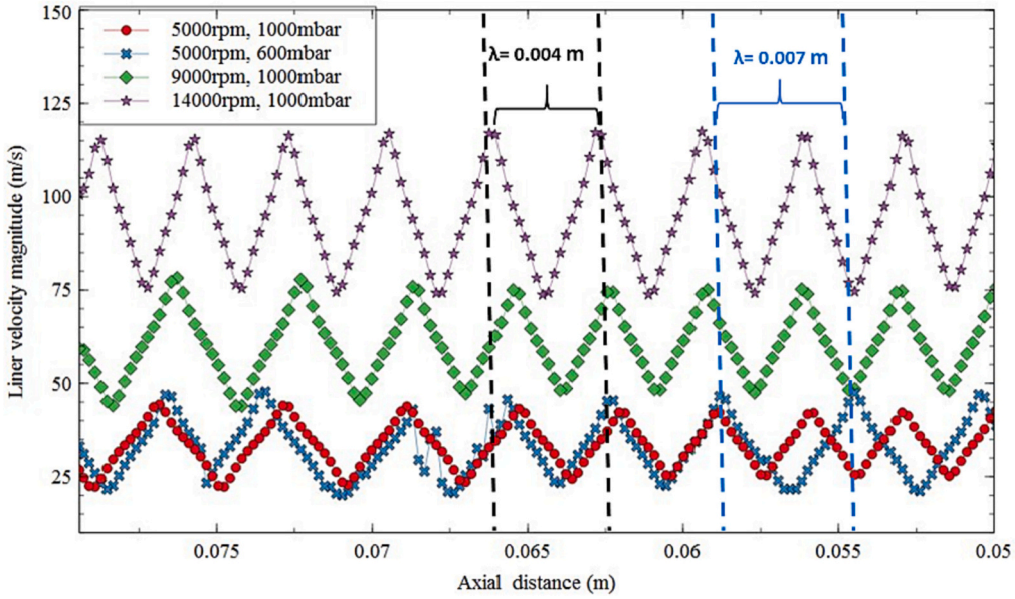

Fig. 15. Taylor vortices wavelength at different rotational speeds and pressures.

8. Flywheel windage losses

The windage losses of an enclosed flywheel are composed of two components; aerodynamic loss due to skin friction, resulting from the viscous forces acting on the outer surface of the flywheel, and aerodynamic loss due to flywheel torque, resulting from the flow interaction between the flywheel sides and the housing. The total windage loss can be determined through the following equation:

$$P = \left(\pi \times L \times C_w \times \rho \times r_i^4 \times \Omega^3\right) + \left(C_m \times \rho \times r_i^5 \times \Omega^3\right) \quad (5)$$

where P is the total windage loss (W), C_w is the drag coefficient due to skin friction on the flywheel top surface, C_m is the flywheel disc torque coefficient, ρ is the air density (kg/m^3), Ω is the flywheel angular velocity (rad/s), r_i is the flywheel radius (m) and L is the flywheel width (m). The drag and torque coefficients, C_w and C_m, respectively, were obtained from the numerical simulations using the average air temperature within the flywheel air-gap. The total windage loss of the flywheel has been calculated at different rotational speeds and pressures as shown in Fig. 17. It is evident that the windage loss increases as the flywheel rotational speed increases due to higher viscous forces acting on the flywheel's outer surface as the speed increases thus generating more heat.

In contrast, windage loss decreases as the pressure decreases, this is mainly attributed to the fact that at partial vacuum, fewer air molecules are present to resist the motion of the flywheel, thus reducing the viscous forces. The results presented in Fig. 17 demonstrate that windage loss can be reduced by up to almost 30 % at 14,000 rpm when the operating pressure is reduced to 600 mbar, which is a substantial reduction in the flywheel windage loss thus leading to higher energy conversion efficiencies. The flywheel system, energy storage and windage loss data under atmospheric conditions are listed in Table 7.

According to the UK's department of transport, in the year 2019, the average car in the UK drove 9200 miles [38] with the average fuel economy of 38.8 miles per gallon, equivalent to 13.7 km per litre of fuel [39]. It has also stated that the average car in the UK emits around 120 g of CO2 per kilometre, equating to an annual CO2 emission of 1777 kg [40]. Assuming that the studied flywheel will be connected to the vehicle mechanically via a CVT with a fixed efficiency of 85 % [41]. A commercial FESS used in light-duty vehicles has approximately a round-trip efficiency of 74 % [42]. The Worldwide Harmonised Light Vehicle Test Procedure (WLTP) cycle is the test procedure used to measure the official fuel consumption and CO_2 emissions for vehicles produced after 2017, which features a typical journey of low, medium and high-speed vehicles. WLTP Class-3 was used in this investigation to measure the potential fuel reduction in an average light weight vehicle in the UK [43]. The fuel savings that can be achieved from using the studied FESS in a light-duty vehicle (1800 kg) is up to 22 % for a WLTP Class-3 cycle, which will lead to a reduction of fuel and CO_2 emissions by 237 L and 390 kg annually, respectively. For every 500,000 new cars sold each year, it is equivalent to a saving of 118.5 million litres of fuel in the first year which will increase with further increase in the number of new cars on the road. In climate change terms, this is equivalent to 195,000 t of CO2 saving in the first year. It is evident that successful mass production of new vehicles with flywheel energy storage technology will provide significant environmental and economic benefits to the community at large.

9. Conclusion

The aerodynamic performance of a flywheel energy storage system was evaluated experimentally and numerically. The numerical results demonstrated the formation of periodic and axisymmetric Taylor vortices within the flywheel annulus. The CFD results revealed that the Taylor vortex cell size increases and becomes more compact when the flywheel speed increases as the flow becomes fully turbulent. This was further confirmed by determining the wavelength of Taylor vortices at different speeds, illustrating vortices travelled a shorter distance as the flywheel speed increased. The experimental and numerical results demonstrated that the temperature of the carbon fibre composite was reduced by >20 % when reducing the operating pressure to 600 mbar. In addition, the windage loss of the flywheel decreased by almost 30 % as the operating pressure was reduced to 600 mbar with windage loss decreasing as the pressure is further reduced. Therefore, higher energy conversion efficiencies can be achieved under partial vacuum provided that adequate bearing seal can be achieved to maintain the pressure inside the flywheel casing. However, it should be noted that the current study has some limitations, such as the simplified geometry used for the numerical analysis, maximum rotational speed of 14,000 rpm and the flywheel target application. Therefore, concrete conclusions cannot be drawn from the results presented in this investigation since the flywheel is designed for light-duty automotive applications; thus, the findings may not be directly applicable to other flywheel designs and sizes.

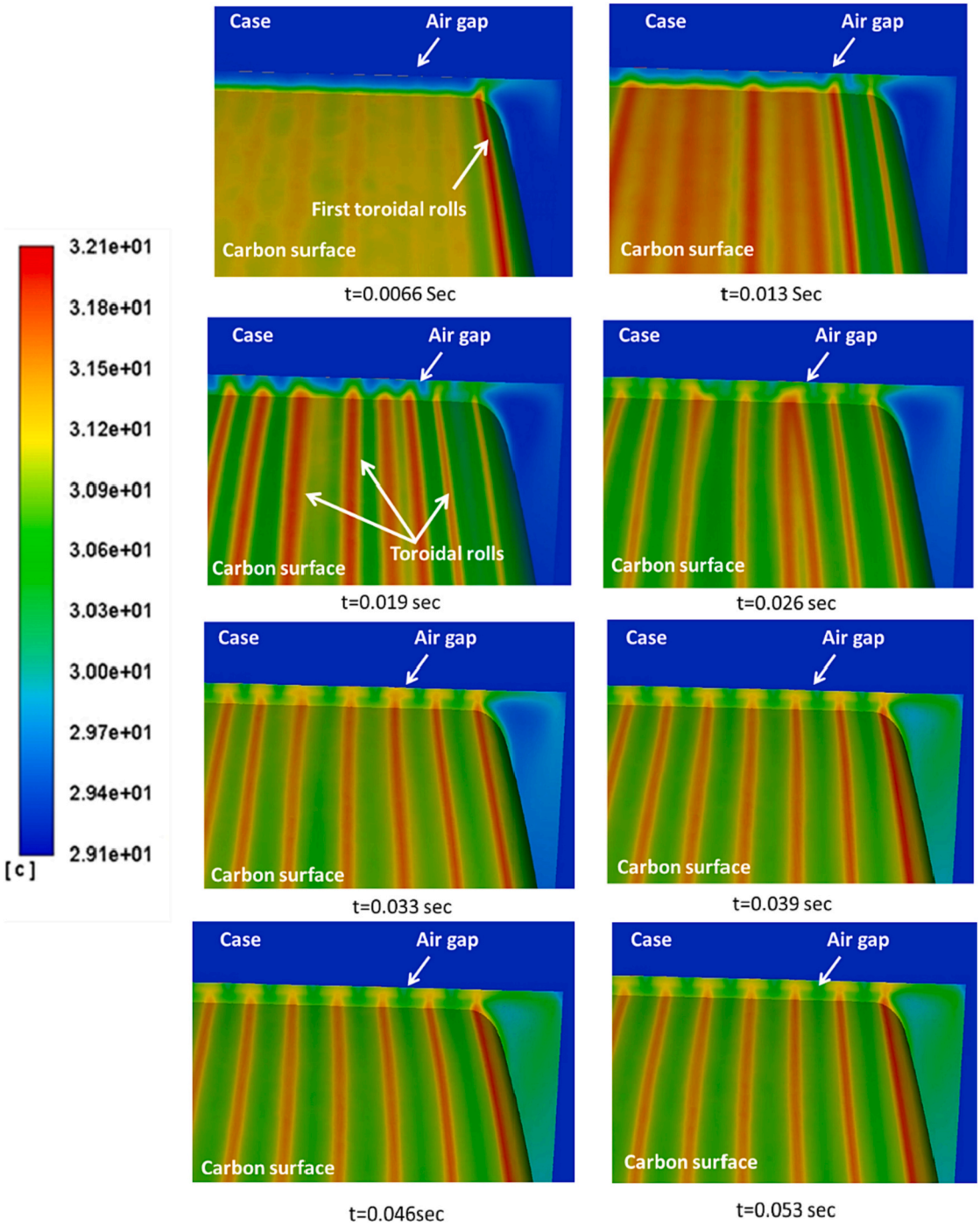

Fig. 16. Temperature contour plots at different time steps illustrating axisymmetric Taylor vortex formation within the flywheel air-gap at the rotational speed and operating pressure of 5000 rpm and 1000 mbar, respectively.

Furthermore, the overall efficiency of the FESS could not be estimated in this study since the aim was to assess the aerodynamic performance of the flywheel itself, therefore the effects of other system components need to be assessed to determine the total system efficiency which may somewhat alter the reported fuel savings.

CRediT authorship contribution statement

Shahed Motaman: Investigation, Software, Formal analysis, Validation, Writing- original draft. **Mahmoud Eltaweel**: Investigation, Software, Formal analysis, Writing- original draft. **Mohammad Reza Herfatmanesh**: Conceptualization, Methodology, Formal analysis, Writing- reviewing and editing, Supervision. **Tobias Knichel**: Investigation, Writing- reviewing and editing. **Andrew Deakin**: Investigation, Writing- reviewing and editing.

Declaration of competing interest

The authors declare that they have no known competing financial interests or personal relationships that could have appeared to influence the work reported in this paper.

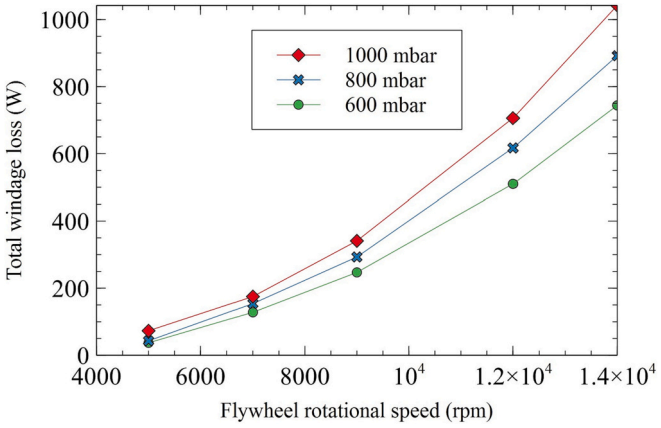

Fig. 17. Flywheel windage loss at different rotational speeds and pressures.

Table 7
Flywheel system parameters.

Rated power	20 kW
Storage capacity	140 kJ
Flywheel weight	13.3 kg
Flywheel inertia	0.13 Kg.m^2
Flywheel windage losses at full speed	1200 W
Flywheel max speed	14,000 rpm

Data availability

Data will be made available on request.

References

[1] E.A. Esparcia, M.T. Castro, C.M.F. Odulio, J.D. Ocon, A stochastic techno-economic comparison of generation-integrated long duration flywheel, lithium-ion battery, and lead-acid battery energy storage technologies for isolated microgrid applications, J. Energy Storage 1 (52) (2022), 104681.

[2] R. Yokoi, T. Watari, M. Motoshita, Future greenhouse gas emissions from metal production: gaps and opportunities towards climate goals, EnergyEnviron. Sci. 15 (1) (2022).

[3] A.J. Cohen, M. Brauer, R. Burnett, H.R. Anderson, J. Frostad, K. Estep, et al., Estimates and 25-year trends of the global burden of disease attributable to ambient air pollution: an analysis of data from the global burden of diseases study 2015, Lancet 389 (10082) (2017).

[4] M. Frumkin, P. Hall, American Dream Cars: 60 Years of the Best Concept Vehicles, 2002.

[5] K. Erhan, E. Özdemir, Prototype production and comparative analysis of high-speed flywheel energy storage systems during regenerative braking in hybrid and electric vehicles, J. Energy Storage 1 (43) (2021), 103237.

[6] X. Li, A. Palazzolo, A review of flywheel energy storage systems: state of the art and opportunities, J. Energy Storage 1 (46) (2022), 103576.

[7] D. Cross, C. Brockbank, Mechanical hybrid system comprising a flywheel and CVT for motorsport and mainstream automotive applications, in: SAE Technical Papers, 2009.

[8] J. Verma, D. Kumar, Recent developments in energy storage systems for marine environment, Materials Advances. 2 (2021).

[9] D. Erdemir, I. Dincer, Assessment of renewable energy-driven and flywheel integrated fast-charging station for electric buses: a case study, J. Energy Storage 1 (30) (2020), 101576.

[10] S. Koohi-Fayegh, M.A. Rosen, A review of energy storage types, applications and recent developments, J. Energy Storage 1 (27) (2020), 101047.

[11] K.R. Pullen, The status and future of flywheel energy storage, Joule 3 (2019).

[12] J. Lenz, B.R.K. Blackman, A.C. Taylor, R. Morgan, C. Crua, Selection of test methods to examine the fracture mechanics of carbon fibre composite flywheels, in: 16th European Conference on Composite Materials, ECCM 2014, 2014.

[13] H.P. Liu, M. Werst, J.J. Hahne, D. Bogard, Prediction of windage losses of an enclosed high speed composite rotor in low air pressure environments, in: Proceedings of the ASME Summer Heat Transfer Conference, 2003.

[14] J. Hahne, M. Werst, C. Penney, H.P. Liu, J. O'Rarden, D. Bogard, Measurement of windage losses and temperature distribution for a high speed composite rotor in a stator assembly at low air pressures, in: Proceedings of the ASME Summer Heat Transfer Conference, 2003.

[15] D. Coren, Childs PRN, C.A. Long, Windage sources in smooth-walled rotating disc systems, Proc Inst Mech Eng C J Mech Eng Sci. 223 (4) (2009).

[16] S.B. Pawar, B.N. Thorat, CFD simulation of Taylor-Couette flow in scraped surface heat exchanger, Chem. Eng. Res. Des. 90 (3) (2012).

[17] M.L. Hosain, R.B. Fdhila, K. Rönnberg, Air-gap flow and thermal analysis of rotating machines using CFD, in: Energy Procedia, 2017.

[18] M. Fénot, Y. Bertin, E. Dorignac, G. Lalizel, A review of heat transfer between concentric rotating cylinders with or without axial flow, Int. J. Therm. Sci. Vol. 50 (2011).

[19] M.L. Hosain, R. Bel Fdhila, K. Rönnberg, Taylor-couette flow and transient heat transfer inside the annulus air-gap of rotating electrical machines, Appl. Energy 207 (2017).

[20] H. Schlichting, Boundary-layer Theory, 7th ed., McGraw-Hill, 1979.

[21] P.R. Fenstermacher, H.L. Swinney, J.P. Gollub, Dynamical instabilities and the transition to chaotic Taylor vortex flow, J. Fluid Mech. 94 (1) (1979).

[22] J.P. Gollub, H.L. Swinney, Onset of turbulence in a rotating fluid, in: Universality in Chaos, Second Edition, 2017.

[23] C. Gazley, Heat transfer characteristics of the rotational and axial flow between concentric cylinders, Trans. ASME. 1 (80) (1958) 79–90.

[24] K.M. Becker, J. Kaye, Measurements of diabatic flow in an annulus with an inner rotating cylinder, J. Heat Transf. 84 (2) (1962).

[25] H. Aoki, H. Nohira, H. Arai, Convective heat transfer in an annulus with an inner rotating cylinder, Bull. JSME 10 (39) (1967).

[26] F. Tachibana, S. Fukui, Convective heat transfer of the rotational and axial flow between two concentric cylinders, Bull. JSME 7 (26) (1964).

[27] D.A. Howey, P.R.N. Childs, A.S. Holmes, Air-gap convection in rotating electrical machines, IEEE Trans. Ind. Electron. Vol. 59 (2012).

[28] K.R. Anderson, J. Lin, C. McNamara, V. Magri, CFD study of forced air cooling and windage losses in a high speed electric motor. Journal of electronics cooling and thermal, Control. 05 (02) (2015).

[29] S. Haddadi, S. Poncet, Turbulence modeling of torsional couette flows, Int. J. Rotat. Mach. 2008 (2008).

[30] S. Viazzo, S. Poncet, Numerical simulation of the flow stability in a high aspect ratio Taylor-couette system submitted to a radial temperature gradient, Comput Fluids. 101 (2014).

[31] M.T. Hamisu, U.S. Umar, A. Sa'ad, FEA and modal analysis of a damped flywheel with unbalanced masses, Available from: Journal of Applications of Modelling and Simulation 4 (2020) 21–30 http://arqiipubl.com/ams.

[32] O. Aydogmus, G. Boztas, R. Celikel, Design and analysis of a flywheel energy storage system fed by matrix converter as a dynamic voltage restorer, Energy 238 (2022).

[33] S.E. Gustafsson, Transient plane source techniques for thermal conductivity and thermal diffusivity measurements of solid materials, Rev. Sci. Instrum. 62 (3) (1991).

[34] H.K. Versteeg, W. Malalasekera, G. Orsi, J.H. Ferziger, A.W. Date, J.D. Anderson, An introduction to computational fluid dynamics - the finite volume method, in: Fluid Flow handbook, McGraw-Hill, 1995.

[35] T. Wang, A brief review on wind turbine aerodynamics, Theor. Appl. Mech. Lett. 2 (6) (2012).

[36] M.A. Kabir, A. Hafiz, Modeling and Simulation of a Supersonic Convergent Divergent Nozzle Using Computational Fluid Dynamics (CFD), 2019.

[37] H. Wang, Experimental and Numerical Study of Taylor-Couette flow, 2015. Graduate Theses and Dissertations.

[38] Vehicle mileage and occupancy - GOV.UK, Available from: https://www.gov.uk/government/statistical-data-sets/nts09-vehicle-mileage-and-occupancy, 2022.

[39] Energy and environment: data tables (ENV) - GOV.UK [Internet], Available from: https://www.gov.uk/government/statistical-data-sets/energy-and-environment-data-tables-env, 2022.

[40] New car carbon dioxide emissions - GOV.UK [Internet], Available from: https://www.gov.uk/government/publications/new-car-carbon-dioxide-emissions, 2022.

[41] R.T. Doucette, M.D. McCulloch, A comparison of high-speed flywheels, batteries, and ultracapacitors on the bases of cost and fuel economy as the energy storage system in a fuel cell based hybrid electric vehicle, J. Power Sources 196 (3) (2011).

[42] C. Brockbank, C. Greenwood, Fuel economy benefits of a flywheel & CVT based mechanical hybrid for city bus and commercial vehicle applications, SAE Int. J. Commer. Veh. 2 (2) (2010).

[43] Worldwide Harmonised Light Vehicle Test Procedure, VCA [Internet], Available from: https://www.vehicle-certification-agency.gov.uk/fuel-consumption-co2/the-worldwide-harmonised-light-vehicle-test-procedure/, 2022.